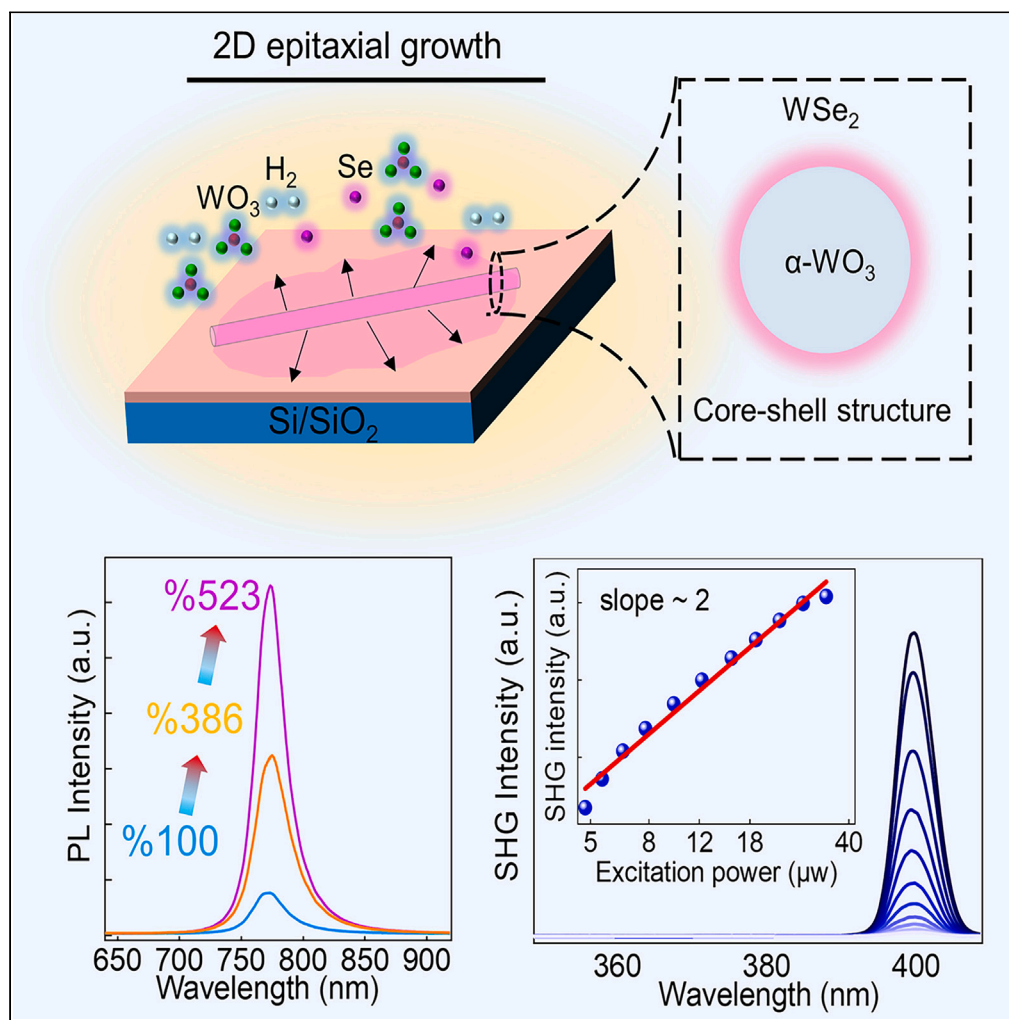**Article**

Directly seeding epitaxial growth of tungsten oxides/tungsten diselenide mixed-dimensional heterostructures with excellent optical properties

Xiang Chen,
Yaqing Zhang,
Xinxin Yue, ...,
Cuntao Gao, Yuan
Yan, Xuewen Fu

yanyuan1314@gmail.com (Y.Y.)
xwfu@nankai.edu.cn (X.F.)

Highlights

A three-step seeding
growth strategy for
constructing mixed-
dimensional
heterostructures

The seeding promoters for
high crystalline quality
WSe$_2$ monolayer epitaxy
growth

The core-shell structure of
WO$_x$ and WSe$_2$ can
enhance the intensity of
nonlinear response

Article

Directly seeding epitaxial growth of tungsten oxides/tungsten diselenide mixed-dimensional heterostructures with excellent optical properties

Xiang Chen,[1,3] Yaqing Zhang,[1,3] Xinxin Yue,[1] Zhuanzhuan Huang,[1] Lifu Zhang,[1] Min Feng,[1] Fang Liu,[1] Cuntao Gao,[1] Yuan Yan,[1,*] and Xuewen Fu[1,2,4,*]

SUMMARY

Mixed-dimensional heterostructures have drawn significant attention due to their intriguing physical properties and potential applications in electronic and optoelectronic nanodevices. However, limited by the lattice matching, the preparation of heterostructures is experimentally difficult and the underlying growth mechanism has not been well established. Here, we report a three-step seeding epitaxial growth strategy for synthesizing mixed-dimensional heterostructures of one-dimensional microwire (MW) and two-dimensional atomic thin film. Our growth strategy has successfully realized direct epitaxial growth of WSe$_2$ film on WO$_x$ MW and significantly improves the quality of the epitaxial WSe$_2$ monolayer, which is evidenced by the remarkably enhanced photoluminescence (PL). More intriguingly, the as-synthesized WO$_x$ MWs exhibit a strong nonlinear optical response due to the enhancement effect of the core (WO$_x$)-shell (WSe$_2$) nanocavity. Our work provides a feasible route for direct growth of WO$_x$-based mixed-dimensional heterostructures, which possess potential applications in high-performance optoelectronic devices.

INTRODUCTION

Heteroepitaxy offers a unique strategy for creating diverse mixed-dimensional heterostructures within a unified monolithic structure.[1–3] One of the common routes to realize this "bottom-up" epitaxial growth is the chemical vapor deposition (CVD), which has been successfully applied to the synthesis of multi-type one-dimensional (1D) nanowires, two-dimensional (2D) thin films, and corresponding lateral heterostructures.[4–8] So far, several 1D-2D hybrid functional materials have been successfully integrated using the CVD method, such as graphene–ZnO,[9] MoS$_2$-BiS$_3$,[10] WS$_2$–Sb$_2$Se$_3$,[11] WS$_2$–CdS,[12] etc. These mixed-dimensional heterostructures hold tremendous promise in the fields of electronics and optoelectronics. In comparison to mechanical stacking or physical transfer methods, CVD heteroepitaxy offers advantages in creating high-quality vertically stacked and in-plane interconnected structures. Additionally, direct vapor epitaxy offers the advantage of circumventing interface contamination and facilitating precise size control through meticulous optimization of growth parameters, allowing the synthesis of large-area heterostructures that can be easily scaled up for practical applications.[13,14]

However, due to the limitation of lattice mismatch and sensitive synthesis conditions, a large number of 1D materials cannot be well integrated with an abundant 2D materials library via the CVD heteroepitaxy method, which inevitably hinders the practical applications, for instance, 1D nanostructured tungsten oxide (WO$_x$), which is well-known for its nonstoichiometric properties and has been perceived as one of the most prominent functional metal oxides for photocatalysis and sensing.[15] The most recent research indicates that WO$_x$ nanowire/WSe$_2$ heterostructures formed by oxygen plasma treatment exhibited high molecular sensitivity and can serve as ultrasensitive molecular sensor.[16] Moreover, Seo et al. have reported the controllable growth of 2D MoS$_2$ nanosheets on 1D WO$_3$ nanorods for improving photoelectrochemical performance,[17] and Lou et al. have constructed 1D/2D heterostructure by growing WO$_{3-x}$ nanowires on the surface of g-C$_3$N$_4$ nanosheets for enhancing photocatalytic activity.[18] All of these studies indicate that realizing the direct large-area growth of 1D-WO$_x$-based mixed-dimensional heterostructures with a feasible route has become one of the most critical issues for their practical applications, which still remains a big challenge.

Here, we introduce a three-step seeding growth strategy involving 1D self-assembly, surface selenization, and 2D epitaxial growth, for the synthesis of 1D-WO$_x$ microwire (MW)/2D-WSe$_2$ film mixed-dimensional heterostructures via a home-built CVD configuration. Optical microscopy (OM) and scanning electron microscopy (SEM) characterizations reveal that the WO$_x$ MWs serve as the seeding centers for the WSe$_2$ monolayer heteroepitaxy growth, resulting in large-area and high-quality mixed-dimensional heterostructures. Combining energy-dispersive X-ray spectroscopy (EDS), selected area electron diffraction (SAED), and Raman and photoluminescence (PL) spectroscopy measurements,
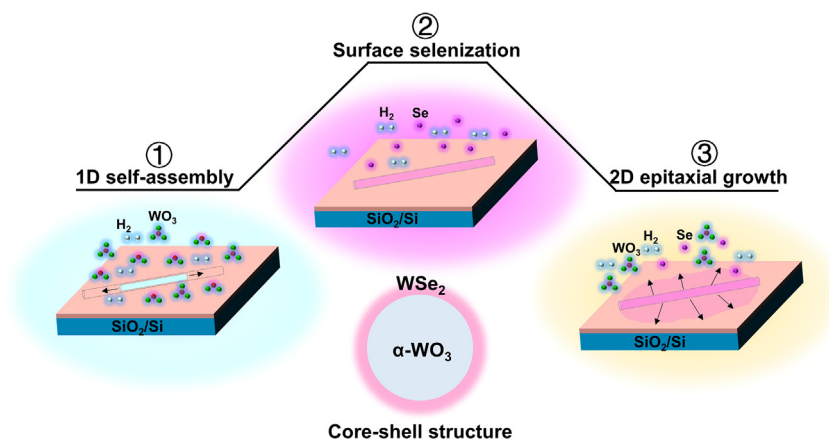
Figure 1. Schematic illustration of the three-step seeding growth strategy of 1D/2D WO$_x$/WSe$_2$ mixed-dimensional heterostructures
The first step is the self-assemble of 1D-WO$_x$ MW under the high mass flux of WO$_3$ precursor, which is marked with ① in the figure. The second step is the surface selenization of as-synthesized WO$_x$ MW under the selenium and hydrogen atmosphere, in which a core (α-WO$_3$)-shell (WSe$_2$) structure is formed (marked with ② in the figure). The third step is the subsequent 2D epitaxial growth of WSe$_2$ film, which is marked with ③ in the figure.

we draw the conclusion that high-quality WSe$_2$ multilayer is formed on the top of the WO$_x$ MWs during the surface selenization process, which is the critical factor to overcome the lattice mismatch and trigger the subsequent 2D seeding epitaxial growth of the WSe$_2$ monolayer. Intriguingly, a strong nonlinear optical response is observed on the top surface of the WO$_x$ MWs after selenization, where the second harmonic generation (SHG) intensity is three orders of magnitude larger than that of the WSe$_2$ monolayer or WO$_x$ MWs under the same excitation condition. We attribute this phenomenon to the enhancement effect of the core (WOx)-shell (WSe$_2$) nanocavity. Moreover, for the monolayer WSe$_2$ formed by such three nucleation mechanisms, we found that the epitaxial WSe$_2$ monolayers grown with the WO$_x$ MW seeds present 3–5 times stronger PL intensity and much smoother surface morphology than the WSe$_2$ monolayers grown by conventional non-seed CVD growth, demonstrating the much higher crystallinity of the WSe$_2$ monolayers synthesized with our three-step seeding growth strategy.

RESULTS AND DISCUSSION

Synthesis and morphology characterizations of mixed-dimensional heterostructures

Figure 1 presents a schematic illustration of the three-step seeding growth strategy proposed in this work, including ① 1D self-assemble process, ② surface selenization, and ③ subsequent 2D epitaxial growth. Based on this three-step seeding growth strategy, we utilized a home-built CVD configuration (Figure S1) which can precisely control the three essential parameters (concentration of Se source, growth pressure, and atmosphere) for growing the WO$_x$/WSe$_2$ mixed-dimensional heterostructures. The basic method is the molten-salt-assisted CVD, which has been widely applied for the synthesis of various two-dimensional transition metal dichalcogenides (TMDs).[19–21] In the first step, the boat containing mixed powder of WO$_3$ and NaCl was subjected to a temperature of 900°C to facilitate a high mass flux through the reaction between molten salts and metal oxides, and then H$_2$/Ar was introduced to provide a reduced atmosphere. As a result, the WO$_3$ was partially reduced and formed volatile WO$_x$ (x < 3) suboxide with the MW morphology via the 1D self-assemble process. Secondly, we turned on the mechanical pump to remove the excess WO$_3$ residues in the quartz tube and introduced the Se source to start the surface selenization. In this process, the surface of the WO$_x$ MW was directly exposed to selenium and hydrogen atmosphere, and multilayer WSe$_2$ film was synthesized by the substitution reaction,[22,23] resulting in a core-shell structure of WO$_x$ MW coated with WSe$_2$ multilayer. To distinguish, we refer to the WO$_x$ MW after selenization treatment as WO$_x$ s-MW. In the third step, we restored the pressure in the quartz tube to atmospheric pressure and held for about 5 min to obtain a stable low mass flow of WO$_3$ and Se sources for the subsequent epitaxial growth of WSe$_2$ monolayer. As TMDs prefer to grow on an existing nucleus,[24–26] the WO$_x$ s-MWs serve as the seeding centers for the lateral growth of the WSe$_2$ monolayer. Finally, the 1D/2D WO$_x$/WSe$_2$ mixed-dimensional heterostructures were successfully synthesized without any transfer or prepattern process. Note that 1D-WO$_x$ MWs and WSe$_2$ single crystals can also be synthesized via this CVD configuration with different recipes; more details can be found in the Method details section.

For comparison, two types of WO$_x$ nanostructures were synthesized without selenization treatment, namely, MWs and micro-cubes (MCs) (Figure 2A). EDS results (Figure S2) illustrate that the elemental compositions of the MWs and MCs are similar, mainly composed of O and W elements. Figure 2B shows the image of the large-scale mixed-dimensional heterostructures containing abundant morphological information. We can clearly observe the formation of WSe$_2$ film surrounding each WO$_x$ s-MW or WO$_x$ s-MC, resulting in two different heterostructures. We define the ensembles with WO$_x$ s-MW or s-MC seed centers as c-type and a-type mixed-dimensional heterostructures, respectively, and their corresponding typical SEM images are shown separately in Figures 2C and 2D, respectively. Typically, the WSe$_2$ monolayers epitaxially grew from the s-MW seed centers tend to be strip shaped and merge together to form continuous films up to hundreds of microns (Figure 2E). In contrast, the WSe$_2$ films epitaxially grew from the s-MC seed centers tend to form isolated circular patterns with an average size of tens of microns (Figure 2F). In addition, there are also some typical triangular WSe$_2$ monolayers without obvious epitaxial seed center, as indicated by
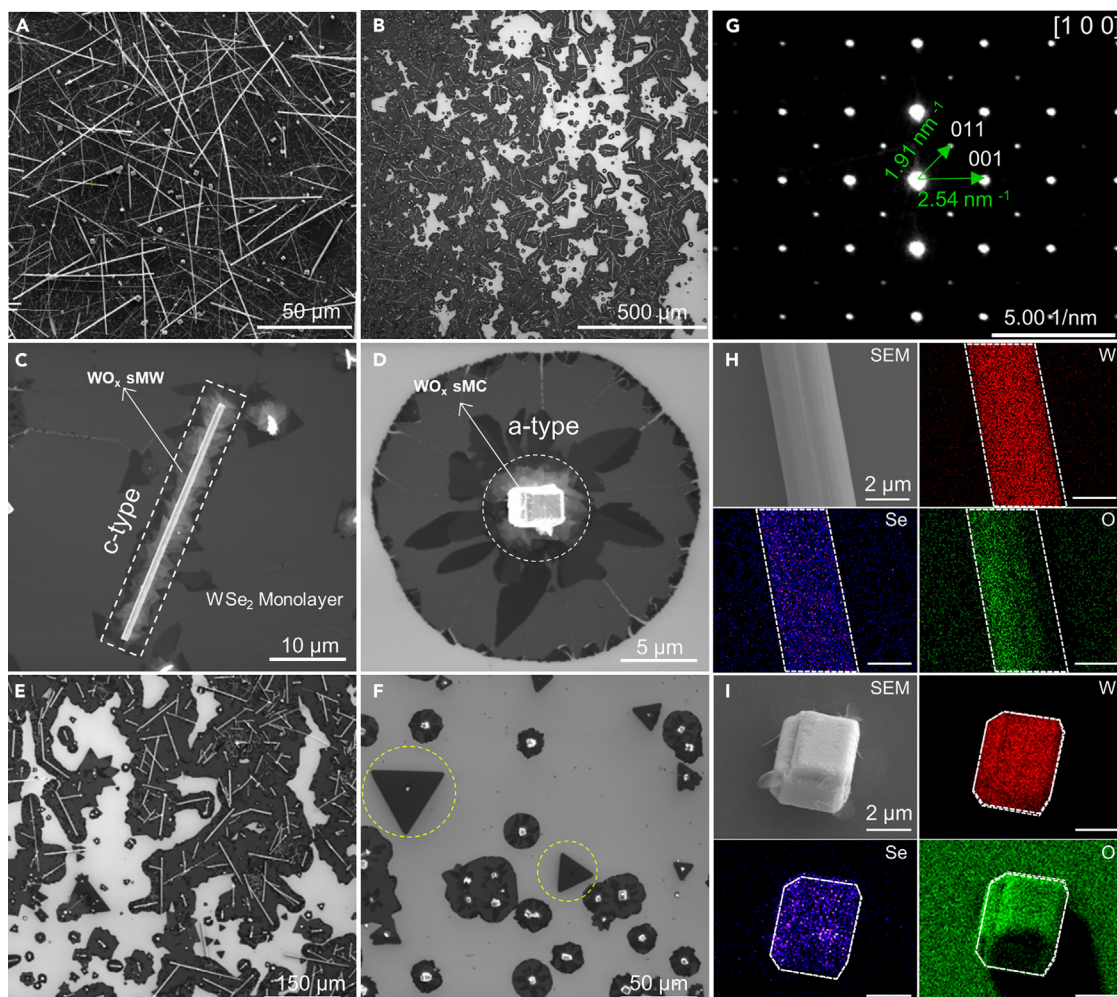
Figure 2. Morphology and structure characterization of mixed-dimensional heterostructures

(A) SEM image of WO_x MW without selenization treatment.

(B) SEM image of large-scale mixed-dimensional heterostructures.

(C) Typical interconnect structure of c-type mixed-dimensional heterostructures.

(D) Typical interconnect structure of a-type mixed-dimensional heterostructures.

(E) Continuously extending c-type mixed-dimensional heterostructures.

(F) Several discrete domains of a-type mixed-dimensional heterostructures.

(G) A typical SAED pattern of c-type WO_x sMW.

(H) EDS elemental mapping of the WO_x s-MW.

(I) EDS elemental mapping of the WO_x s-MC.

the yellow dashed circles in Figure 2F. It seems the crystal orientation of the seed centers has no significant effect on the orientation of the epitaxial results. The reason is that the multilayer WSe_2 film formed on the surface of the WO_x crystal is typically polycrystalline and lacks uniform crystal orientation. Apparently, the geometry of the seeding growth WSe_2 films is significantly affected by the type of the central nucleus. This result is inconsistent with the defect-induced co-nucleus growth mode, in which the WSe_2 film will maintain its own geometric shape during the growth process.[10] Thus the WSe_2 films grow epitaxially on the WO_x s-MWs (or s-MCs) rather than their co-nucleus. Moreover, disordered morphology of WSe_2 multilayer film (indicate by the white dotted line in Figures 2C and 2D) was formed at the contacting region of the mixed-dimensional heterostructure, illustrating the higher chemical reactivity at the contacting region as the seeding promoters can substantially reduce the surface energy of the substrate.[24,25] Thus, the type and placement direction of the WO_x seeds determine the final morphology of the epitaxial WSe_2 monolayer.

We employed high-resolution transmission electron microscopy (HRTEM) and SAED to characterize the crystal structure of the WO_x s-MWs. Figure S3 shows the HRTEM image of a WO_x s-MW, indicating that the predominate growth direction is along the [001] axis. The corresponding SAED pattern shown in Figure 2G indicates its single crystalline nature. By systematic analysis of the diffraction spots, the (001) and
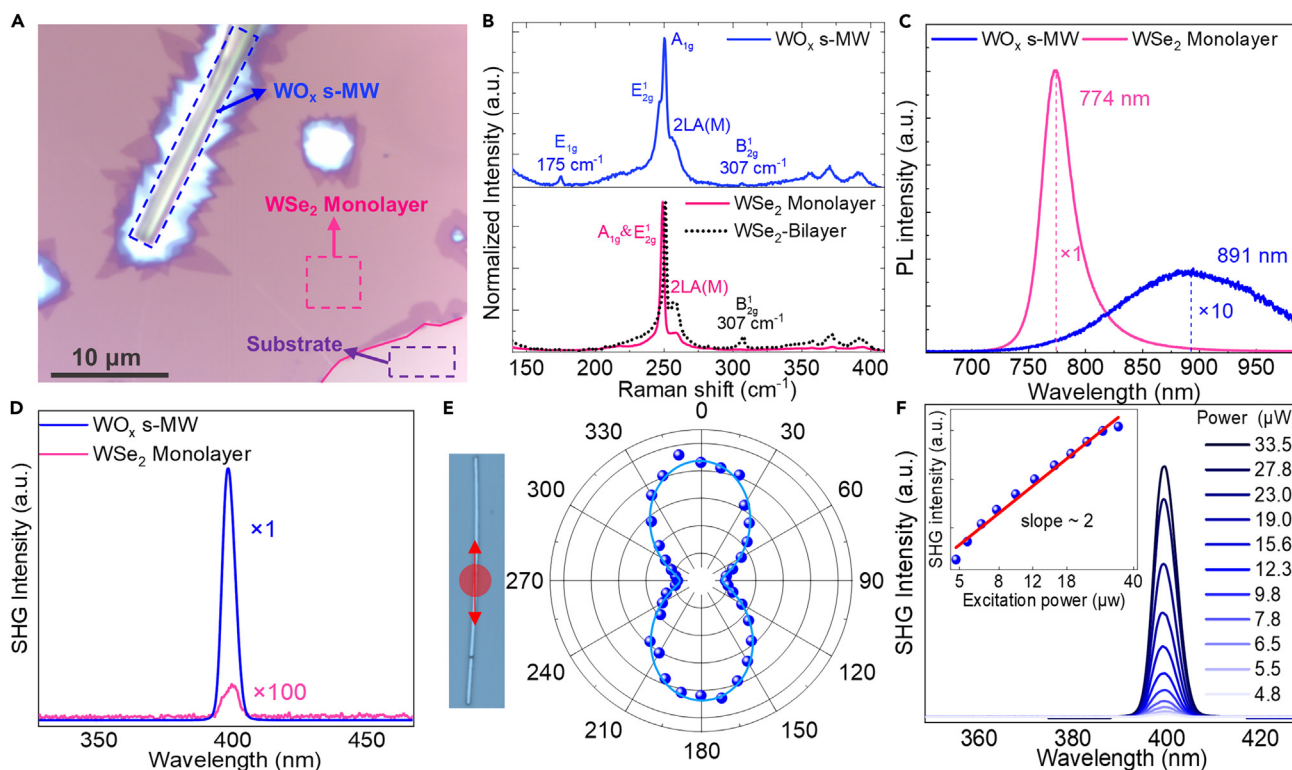
Figure 3. Optical characterizations of the mixed-dimensional heterostructures

(A) OM image of a c-type mixed-dimensional heterostructure.

(B) Raman spectra of the WO_x s-MW and WSe_2 film, respectively.

(C) PL spectra of the WO_x s-MW and WSe_2 monolayer, respectively.

(D) The SHG spectra of WO_x s-MW and WSe_2 monolayer under 800 nm pulsed-laser excitation, respectively.

(E) Polarization dependent SHG patterns measured on the WO_x s-MW, where the inset shows the OM image of the corresponding sample and the red arrow indicates the initial polarization direction of the excitation laser.

(F) The SHG intensity of the WO_x s-MW as a function of excitation power, where the inset shows the fitted line of power-dependent SHG intensity with a slope of 2 in a double logarithmic plot.

(011) lattice plane spacings were determined to be 0.394 nm and 0.524 nm, respectively, in good agreement with the lattice structure of α-WO_3.[15] Since the WO_x s-MWs are relatively thick, the corresponding HRTEM and SAED results mainly reflect their internal lattice structures (similar for s-MCs), which retain the α-WO_3 lattice structure. This is consistent with what we previously described in the synthetic strategy section: only the surface of the WO_x MWs (or MCs) will be selenified. We then used EDS to identify the element composition of the WO_x s-MWs and s-MCs, as shown in Figures 2H and 2I, respectively. The EDS results reveal the co-existence of W, O, and Se elements in the WO_x s-MWs and s-MCs. We note that the Se and W elements exhibit a uniform distribution, while the O element is significantly unevenly distributed, which could be attributed to the shadow effect caused by unevenness of the sample in the EDS measurement. The proportion of Se element in overall composition is around 2% in all the samples, while the proportion of O and W varies from sample to sample. In general, limited by the diffusion depth of Se element in the WO_x crystal, only a small amount of Se element can enter the interior, resulting in a relatively low overall proportion of Se element, which further confirms the existence and rationality of surface selenization process in the growth.

Optical properties of mixed-dimensional heterostructures

We then studied the optical properties of the as-prepared mixed-dimensional heterostructures. Figure 3A shows a typical OM image of the area including mixed-dimensional heterostructure and epitaxial growth WSe_2 monolayer. The WO_x s-MW, WSe_2 monolayer, and bare substrate are indicated by the blue, pink, and purple dotted box, respectively. The Raman spectrum (pink curve in the bottom panel of Figure 3B) collected from the monolayer WSe_2 shows a dominant peak near 250 cm^{-1}, corresponding to the E^1_{2g} and A_{1g} modes (hard to distinguish in a few-layers WSe_2).[27] The broad shoulder near 260 cm^{-1} is assigned as the 2LA(M) Raman mode.[28] For the bilayer WSe_2 (black dashed curve in the bottom panel of Figure 3B), an extra peak at 307 cm^{-1} appears, which is in accordance with B^1_{2g} mode and is a hallmark of few-layer WSe_2.[29] We have further performed Raman measurement on the WO_x s-MW, as shown in the top panel of Figure 3B. The specific fingerprints attained from the Raman spectrum imply that only Raman-active modes related to WSe_2 multilayer exist. Additionally, we observed the E_{1g} (175 cm^{-1}) mode that is forbidden in backscattering experiments on (001) surface of WSe_2 single crystal.[30] Meanwhile, the Raman spectrum

(Figure S4B) has also been measured for the WO$_x$ s-MC (Figure S4A), which shows the similar result. It should be noted that the laser spot size used for our Raman spectroscopy measurement is about 500 nm, smaller than the diameter of the WO$_x$ s-MWs (larger than 1 μm). Therefore, the possibility of the collected Raman signal originating from the multilayer film near the WO$_x$ s-MW (indicated by the white dotted line in Figures 2C and 2D) can be excluded. This indicates that the WO$_x$ s-MWs possess the same Raman fingerprints as the WSe$_2$ multilayer. Besides that, before the selenization we can observe clearly the O-W-O and W=O related Raman modes in the WO$_x$ MWs (Figure S5) without any observable WSe$_2$-related Raman modes.[31,32] The Raman mapping results of WO$_x$ s-MW are shown in Figure S6, revealing a uniform distribution of the WSe$_2$ multilayers on the surface of the WO$_x$ s-MW. Figure 3C shows the PL spectra of the monolayer WSe$_2$ and WO$_x$ s-MW. An intensity peak at ∼774 nm is observed for the monolayer WSe$_2$, which agrees well with the reported A exciton emission of the monolayer WSe$_2$.[33,34] In contrast, the PL spectrum of WO$_x$ s-MW shows a wide spectrum range centered at ∼891 nm with much lower intensity. Because WO$_x$ s-MW does not generate any PL under the excitation of 532 nm laser,[15] this weak PL peak could be ascribed to the WSe$_2$ multilayer on the surface of the WO$_x$ s-MW. All the aforementioned experimental results confirm that the surface layer of the WO$_x$ s-MW is WSe$_2$ multilayer. According to the PL peak position of this emission, we can estimate that the thickness of the WSe$_2$ multilayer on the top surface of the WO$_x$ s-MW is about 170 nm[35]

We further measured the SHG response of the WO$_x$ s-MW. As shown in Figure 3D, with 800 nm fs pulse-laser excitation, the WO$_x$ s-MW exhibits a sharp peak at 400 nm as expected from SHG, which is about three orders of magnitude larger than that of the WSe$_2$ monolayer under the same excitation power. To determine the relationship between the SHG response and the orientation of the WO$_x$ s-MW, polarization-dependent SHG measurements were conducted (Figure 3E). The results reveal a great contrast in the parallel component of the SHG intensity along the growth direction of the WO$_x$ s-MW. We also measured the SHG spectra as a function of excitation power (Figure 3F); the fitted line shows a slope of ∼2 in a double logarithmic plot, verifying the second-order nonlinear optical process.[36] Figure S7 show SHG spectra of both the WO$_x$ MW and WSe$_2$ monolayer, and only a very weak SHG response is observed in WO$_x$ MW. This observed high gain of the SHG response with c-axis polarization dependence in the WO$_x$ s-MW is unusual and cannot be solely attributed to the WSe$_2$ multilayer on the top surface. Therefore, we speculate that the resonance of core-shell nanocavity which is composed of the surface WSe$_2$ multilayer and the internal WO$_x$ MW leads to such enormous signal enhancement. Such similar phenomenon has also been observed in other forms of core-shell nanostructures.[37,38]

Enhanced crystal quality of the seeding growth WSe$_2$ films

To evaluate the crystal quality of the seeding growth WSe$_2$ films, we statistically analyzed more than 300 PL spectra of each type of WSe$_2$ monolayer (non-center, a-type, and c-type) under the same experimental conditions, where all the measured points were randomly selected on the same sample. The statistical histograms presented in Figure 4 (A to C) show the distributions of the total PL intensity and the full width at half maximum (FWHM) that is extracted from the corresponding PL spectra. Among the three types of the epitaxially grown WSe$_2$ monolayer, the non-center type (Figure 4A) has the lowest average PL intensity value (∼10,020, with the unit of a.u) and maximum average FWHM (∼34.4 nm). For the a-center and c-center types (Figures 4B and 4C), their PL intensities show a significant improvement with the average values of 38,710 and 52,470, respectively, meanwhile their FWHMs show a clear decrease with the average values of 31.6 nm and 30.3 nm, respectively. As shown by the typical PL spectra of the three kind samples in Figure 4D, compared with the non-center type, there is a 386% and 532% enhancement for the a-type and c-type monolayers, respectively. The stronger PL intensity and smaller FWHM usually indicate the higher crystal quality of the WSe$_2$ films.[39] Moreover, according to the PL mapping results of the different types of WSe$_2$ monolayers, we found that the seeding growth WSe$_2$ films have a more homogeneous PL intensity distribution (Figure S8) with smoother surface and stronger luminescence (Figure S9). All of these results demonstrate that utilizing WO$_x$ s-MW as an epitaxial center can significantly improve the quality of the epitaxial WSe$_2$ films.

Generally, due to the lattice mismatch, it is difficult to realize direct epitaxial growth of the WSe$_2$ film on WO$_x$ single crystal. However, in the case of WO$_x$ s-MW, the multilayer WSe$_2$ formed on its top surface can overcome this mismatch and trigger the subsequent epitaxial growth of the WSe$_2$ monolayer. The key characteristic of such seeding epitaxy is the bulk single-crystal-like crystalline quality of the epitaxial WSe$_2$ monolayer.[14] To provide further comparison, we also measured the PL spectrum of an exfoliated WSe$_2$ monolayer on SiO$_2$ substrate (Figure S10A). As depicted in Figure S10B, the PL intensity of the c-type WSe$_2$ monolayer is essentially equivalent to that of the exfoliated monolayer. However, there is a noticeable increase in the FWHM values, which rose from 20.1 nm (exfoliated WSe$_2$ monolayer) to 27.1 nm (c-type WSe$_2$ monolayer), accompanied by a redshift in the peak position from 746.9 nm to 777.6 nm. This redshift and broadening of the PL spectrum can be attributed to the inherent built-in tensile strain in the CVD-grown 2D films on oxidized silicon substrates.[40,41] Based on these observations, we can conclude that the c-type WSe$_2$ monolayer exhibits bulk single-crystal-like crystalline quality.

Conclusions

In summary, we have reported a three-step seeding growth strategy for the fabrication of large-scale 1D/2D WO$_x$ MW/WSe$_2$ film mixed-dimensional heterostructures via a specific CVD method. Various characterization techniques, including SEM, EDS, TEM, Raman, and PL, have been employed to analyze the morphology, element composition, and crystal structure of the synthesized heterostructures. We have confirmed the existence of WSe$_2$ multilayer on the top surface of WO$_x$ s-MWs, which plays a crucial role in the formation of mixed-dimensional heterostructures. The growth mechanism implies the WO$_x$ s-MWs can serve as the seeding promoters for high crystalline quality of WSe$_2$ monolayer epitaxy growth, because the WSe$_2$ multilayer at its surface can serve as a template to overcome the lattice mismatch and significantly improve the crystalline quality of the epitaxial WSe$_2$ film. More intriguingly, the WO$_x$ s-MWs show a significant SHG response with
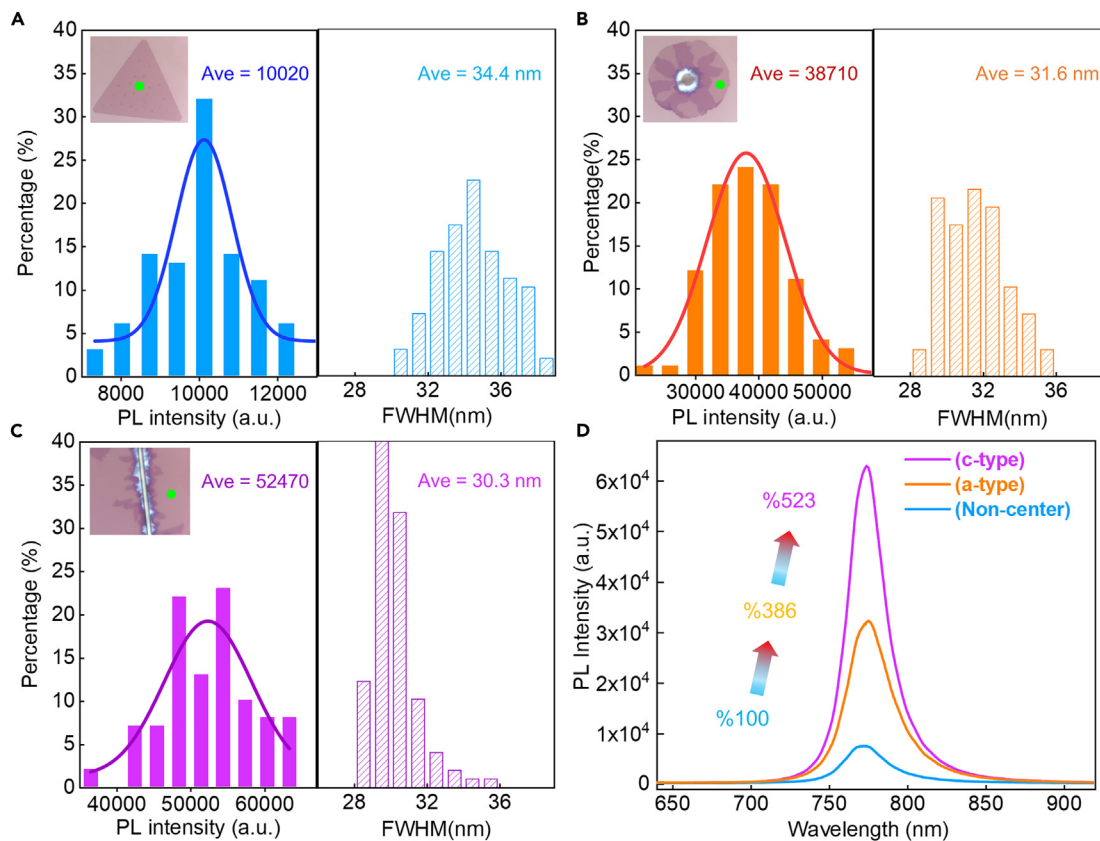
Figure 4. Comparison of statistic distributions of PL intensity and FWHM for three types of WSe₂ monolayer

(A–C) The statistic distributions of PL intensity (left) and FWHM (right) for non-center type WSe$_2$ monolayer, a-type WSe$_2$ monolayer, and c-type WSe$_2$ monolayer, respectively. The corresponding OM images of the samples are shown in the insets. The solid lines are Gaussian fit to the probability distributions.

(D) Representative PL spectra of the three types of WSe$_2$ monolayer under the same excitation power.

polarization dependence due to the special core-shell structure. The mixed-dimensional heterostructures possess excellent optical properties, highlighting their potential for applications in future electronic and optoelectronic devices.

Limitations of the study

In the present work, we successfully synthesized the heterostructure of 1D-WO$_x$ MW and 2D-WSe$_2$ atomic thin film through the CVD method. However, it is currently impossible to characterize the coupling strength of this structure and the corresponding device is difficult to obtain. In our future studies, we intend to seek cooperation in performance characterization and device preparation.

STAR★METHODS

Detailed methods are provided in the online version of this paper and include the following:

- KEY RESOURCES TABLE
- RESOURCE AVAILABILITY
  - Lead contact
  - Materials availability
  - Data and code availability
- EXPERIMENTAL MODEL AND STUDY PARTICIPANT DETAILS
- METHOD DETAILS
  - Synthesis of the WO$_x$/WSe$_2$ heterostructures
  - Characterizations of WO$_x$ s-MW and WSe$_2$ film
  - Nonlinear optical performance measurements
- QUANTIFICATION AND STATISTICAL ANALYSIS
- ADDITIONAL RESOURCES

SUPPLEMENTAL INFORMATION

Supplemental information can be found online at https://doi.org/10.1016/j.isci.2023.108296.

AUTHOR CONTRIBUTIONS

X.F. and X.C. conceived the research project. X.C., X.Y., and Z.H. did the experimental measurements. X.C. and Y.Z. proceeded data analysis. X.C. and Y.Z. wrote the manuscript with input from X.F. All the authors contributed to the discussion and revision of the manuscript.

DECLARATION OF INTERESTS

The authors declare no conflicts of interest.

REFERENCES

1. Huang, P.-Y., Qin, J.-K., Zhu, C.-Y., Zhen, L., and Xu, C.-Y. (2021). 2D-1D mixed-dimensional heterostructures: progress, device applications and perspectives. J. Phys. Condens. Matter 33, 493001. https://doi.org/10.1088/1361-648X/ac2388.

2. Bae, S.H., Lu, K., Han, Y., Kim, S., Qiao, K., Choi, C., Nie, Y., Kim, H., Kum, H.S., Chen, P., et al. (2020). Graphene-assisted spontaneous relaxation towards dislocation-free heteroepitaxy. Nat. Nanotechnol. 15, 272–276. https://doi.org/10.1038/s41565-020-0633-5.

3. Chu, Y.-H. (2017). Van der Waals oxide heteroepitaxy. npj Quantum Mater. 2, 67. https://doi.org/10.1038/s41535-017-0069-9.

4. Barrigón, E., Heurlin, M., Bi, Z., Monemar, B., and Samuelson, L. (2019). Synthesis and Applications of III-V Nanowires. Chem. Rev. 119, 9170–9220. https://doi.org/10.1021/acs.chemrev.9b00075.

5. Zhang, Y., Yao, Y., Sendeku, M.G., Yin, L., Zhan, X., Wang, F., Wang, Z., and He, J. (2019). Recent Progress in CVD Growth of 2D Transition Metal Dichalcogenides and Related Heterostructures. Adv. Mater. 31, e1901694. https://doi.org/10.1002/adma.201901694.

6. Chen, K., Wan, X., and Xu, J. (2017). Epitaxial Stitching and Stacking Growth of Atomically Thin Transition-Metal Dichalcogenides (TMDCs) Heterostructures. Adv. Funct. Mater. 27, 1603884. https://doi.org/10.1002/adfm.201603884.

7. Cui, Y., Li, B., Li, R., and Wei, Z. (2017). Chemical vapor deposition growth of two-dimensional heterostructures. SCI CHINA PHYS MECH 1, 1–13. https://doi.org/10.1007/s11433-017-9105-x.

8. Li, M.Y., Shi, Y., Cheng, C.C., Lu, L.S., Lin, Y.C., Tang, H.L., Tsai, M.L., Chu, C.W., Wei, K.H., He, J.H., et al. (2015). Epitaxial growth of a monolayer WSe2-MoS2 lateral pn junction with an atomically sharp interface. Science 349, 524–528. https://doi.org/10.1126/science.aab4097.

9. Park, J.B., Oh, H., Park, J., Kim, N.J., Yoon, H., and Yi, G.C. (2016). Scalable ZnO nanotube arrays grown on CVD-graphene films. Apl. Mater. 4, 106104. https://doi.org/10.1063/1.4964490.

10. Li, Y., Huang, L., Li, B., Wang, X., Zhou, Z., Li, J., and Wei, Z. (2016). Co-nucleus 1D/2D Heterostructures with Bi2S3 Nanowire and MoS2 Monolayer: One-Step Growth and Defect-Induced Formation Mechanism. ACS Nano 10, 8938–8946. https://doi.org/10.1021/acsnano.6b04952.

11. Sun, G., Li, B., Li, J., Zhang, Z., Ma, H., Chen, P., Zhao, B., Wu, R., Dang, W., Yang, X., et al. (2019). Direct van der Waals epitaxial growth of 1D/2D Sb2Se3/WS2 mixed-dimensional p-n heterostructures. Nano Res. 12, 1139–1145. https://doi.org/10.1007/s12274-019-2364-1.

12. Gong, Y., Zhang, X., Yang, T., Huang, W., Liu, H., Liu, H., Zheng, B., Li, D., Zhu, X., Hu, W., and Pan, A. (2019). Vapor growth of CdS nanowires/WS2 nanosheet heterostructures with sensitive photodetection. Nanotechnology 30, 345603. https://doi.org/10.1088/1361-6528/ab1f3c.

13. Wang, Q., Li, N., Tang, J., Zhu, J., Zhang, Q., Jia, Q., Lu, Y., Wei, Z., Yu, H., Zhao, Y., et al. (2020). Wafer-Scale Highly Oriented Monolayer MoS2 with Large Domain Sizes. Nano Lett. 20, 7193–7199. https://doi.org/10.1021/acs.nanolett.0c02531.

14. Xu, X., Pan, Y., Liu, S., Han, B., Gu, P., Li, S., Xu, W., Peng, Y., Han, Z., Chen, J., et al. (2021). Seeded 2D epitaxy of large-area single-crystal films of the van der Waals semiconductor 2H MoTe(2). Science 372, 195–200. https://doi.org/10.1126/science.abf5825.

15. Zheng, H., Ou, J.Z., Strano, M.S., Kaner, R.B., Mitchell, A., and Kalantar-zadeh, K. (2011). Nanostructured Tungsten Oxide - Properties, Synthesis, and Applications. Adv. Funct. Mater. 21, 2175–2196. https://doi.org/10.1002/adfm.201002477.

16. Lv, Q., Tan, J., Wang, Z., Gu, P., Liu, H., Yu, L., Wei, Y., Gan, L., Liu, B., Li, J., et al. (2023). Ultrafast charge transfer in mixed-dimensional WO(3-x) nanowire/WSe(2) heterostructures for attomolar-level molecular sensing. Nat. Commun. 14, 2717. https://doi.org/10.1038/s41467-023-38198-x.

17. Seo, D.-B., Dongquoc, V., Jayarathna, R.A., Lee, S., Lee, J.-H., and Kim, E.-T. (2022). Rational heterojunction design of 1D WO3 nanorods decorated with vertical 2D MoS2 nanosheets for enhanced photoelectrochemical performance. J. Alloys Compd. 911, 165090. https://doi.org/10.1016/j.jallcom.2022.165090.

18. Lou, Z., and Xue, C. (2016). In situ growth of WO3−xnanowires on g-C3N4nanosheets: 1D/2D heterostructures with enhanced photocatalytic activity. CrystEngComm 18, 8406–8410. https://doi.org/10.1039/c6ce01557c.

19. Li, S., Wang, S., Tang, D.-M., Zhao, W., Xu, H., Chu, L., Bando, Y., Golberg, D., and Eda, G. (2015). Halide-assisted atmospheric pressure growth of large WSe2 and WS2 monolayer crystals. Appl. Mater. Today 1, 60–66. https://doi.org/10.1016/j.apmt.2015.09.001.

20. Zhou, J., Lin, J., Huang, X., Zhou, Y., Chen, Y., Xia, J., Wang, H., Xie, Y., Yu, H., Lei, J., et al. (2018). A library of atomically thin metal chalcogenides. Nature 556, 355–359. https://doi.org/10.1038/s41586-018-0008-3.

21. Huang, L., Hu, Z., Jin, H., Wu, J., Liu, K., Xu, Z., Wan, J., Zhou, H., Duan, J., Hu, B., and Zhou, J. (2020). Salt-Assisted Synthesis of 2D Materials. Adv. Funct. Mater. 30, 1908486. https://doi.org/10.1002/adfm.201908486.

22. Browning, P., Eichfeld, S., Zhang, K., Hossain, L., Lin, Y.-C., Wang, K., Lu, N., Waite, A.R., Voevodin, A.A., Kim, M., and Robinson, J.A. (2015). Large-area synthesis of WSe2 from WO3 by selenium–oxygen ion exchange. 2D

Mater. *2*, 014003. https://doi.org/10.1088/2053-1583/2/1/014003.

23. Kim, H., Yun, S.J., Park, J.C., Park, M.H., Park, J.H., Kim, K.K., and Lee, Y.H. (2015). Seed growth of tungsten diselenide nanotubes from tungsten oxides. Small *11*, 2192–2199. https://doi.org/10.1002/smll.201403279.

24. Ling, X., Lee, Y.H., Lin, Y., Fang, W., Yu, L., Dresselhaus, M.S., and Kong, J. (2014). Role of the seeding promoter in MoS2 growth by chemical vapor deposition. Nano Lett. *14*, 464–472. https://doi.org/10.1021/nl4033704.

25. Li, Y., Hao, S., DiStefano, J.G., Murthy, A.A., Hanson, E.D., Xu, Y., Wolverton, C., Chen, X., and Dravid, V.P. (2018). Site-Specific Positioning and Patterning of MoS(2) Monolayers: The Role of Au Seeding. ACS Nano *12*, 8970–8976. https://doi.org/10.1021/acsnano.8b02409.

26. Wang, Z., Huang, Q., Chen, P., Guo, S., Liu, X., Liang, X., and Wang, L. (2016). Metal Induced Growth of Transition Metal Dichalcogenides at Controlled Locations. Sci. Rep. *6*, 38394. https://doi.org/10.1038/srep38394.

27. Luo, X., Zhao, Y., Zhang, J., Toh, M., Kloc, C., Xiong, Q., and Quek, S.Y. (2013). Effects of lower symmetry and dimensionality on Raman spectra in two-dimensional WSe2. Phys. Rev. B *88*, 195313. https://doi.org/10.1103/PhysRevB.88.195313.

28. Zhao, W., Ghorannevis, Z., Amara, K.K., Pang, J.R., Toh, M., Zhang, X., Kloc, C., Tan, P.H., and Eda, G. (2013). Lattice dynamics in mono- and few-layer sheets of WS2 and WSe2. Nanoscale *5*, 9677–9683. https://doi.org/10.1039/C3NR03052K.

29. Yamamoto, M., Dutta, S., Aikawa, S., Nakaharai, S., Wakabayashi, K., Fuhrer, M.S., Ueno, K., and Tsukagoshi, K. (2015). Self-limiting layer-by-layer oxidation of atomically thin WSe2. Nano Lett. *15*, 2067–2073. https://doi.org/10.1021/nl5049753.

30. Sahin, H., Tongay, S., Horzum, S., Fan, W., Zhou, J., Li, J., Wu, J., and Peeters, F.M. (2013). Anomalous Raman spectra and thickness-dependent electronic properties of WSe2. Phys. Rev. B *87*, 165409. https://doi.org/10.1103/PhysRevB.87.165409.

31. Thummavichai, K., Wang, N., Xu, F., Rance, G., Xia, Y., and Zhu, Y. (2018). In situ investigations of the phase change behaviour of tungsten oxide nanostructures. R. Soc. Open Sci. *5*, 171932. https://doi.org/10.1098/rsos.171932.

32. Garcia-Sanchez, R.F., Ahmido, T., Casimir, D., Baliga, S., and Misra, P. (2013). Thermal effects associated with the Raman spectroscopy of WO3 gas-sensor materials. J. Phys. Chem. A *117*, 13825–13831. https://doi.org/10.1021/jp408303p.

33. Zhao, W., Ghorannevis, Z., Chu, L., Toh, M., Kloc, C., Tan, P.H., and Eda, G. (2013). Evolution ofElectronic Structure in Atomically Thin Sheets of WS2 andWSe2. ACS Nano *7*, 791–797. https://doi.org/10.1021/nn305275h.

34. Huang, J.K., Pu, J., Hsu, C.L., Chiu, M.H., Juang, Z.Y., Chang, Y.H., Chang, W.H., Iwasa, Y., Takenobu, T., and Li, L.J. (2014). Large-area synthesis of highly crystalline WSe2 monolayers and device applications. ACS Nano *8*, 923–930. https://doi.org/10.1021/nn405719x.

35. Li, Y., Liu, W., Xu, H., Chen, H., Ren, H., Shi, J., Du, W., Zhang, W., Feng, Q., Yan, J., et al. (2019). Unveiling Bandgap Evolution and Carrier Redistribution in Multilayer WSe2 : Enhanced Photon Emission via Heat Engineering. Adv. Opt. Mater. *8*, 1901226. https://doi.org/10.1002/adom.201901226.

36. Zhang, D., Zeng, Z., Tong, Q., Jiang, Y., Chen, S., Zheng, B., Qu, J., Li, F., Zheng, W., Jiang, F., et al. (2020). Near-Unity Polarization of Valley-Dependent Second-Harmonic Generation in Stacked TMDC Layers and Heterostructures at Room Temperature. Adv. Mater. *32*, 1908061. https://doi.org/10.1002/adma.201908061.

37. Zielinski, M., Oron, D., Chauvat, D., and Zyss, J. (2009). Second-harmonic generation from a single core/shell quantum dot. Small *5*, 2835–2840. https://doi.org/10.1002/smll.200900399.

38. Pu, Y., Grange, R., Hsieh, C.L., and Psaltis, D. (2010). Nonlinear optical properties of core-shell nanocavities for enhanced second-harmonic generation. Phys. Rev. Lett. *104*, 207402. https://doi.org/10.1103/PhysRevLett.104.207402.

39. Shi, W., Lin, M.-L., Tan, Q.-H., Qiao, X.-F., Zhang, J., and Tan, P.-H. (2016). Raman and photoluminescence spectra of two-dimensional nanocrystallites of monolayer WS2 and WSe2. 2D Mater. *3*, 025016. https://doi.org/10.1088/2053-1583/3/2/025016.

40. Ahn, G.H., Amani, M., Rasool, H., Lien, D.H., Mastandrea, J.P., Ager Iii, J.W., Dubey, M., Chrzan, D.C., Minor, A.M., and Javey, A. (2017). Strain-engineered growth of two-dimensional materials. Nat. Commun. *8*, 608. https://doi.org/10.1038/s41467-017-00516-5.

41. Sortino, L., Brooks, M., Zotev, P.G., Genco, A., Cambiasso, J., Mignuzzi, S., Maier, S.A., Burkard, G., Sapienza, R., and Tartakovskii, A.I. (2020). Dielectric Nanoantennas for Strain Engineering in Atomically Thin Two-Dimensional Semiconductors. ACS Photonics *7*, 2413–2422. https://doi.org/10.1021/acsphotonics.0c00294.

STAR★METHODS

KEY RESOURCES TABLE

REAGENT or RESOURCE	SOURCE	IDENTIFIER
Chemicals, peptides, and recombinant proteins		
Sodium chloride	Sigma-Aldrich	CAS #7647-14-5
Tungsten oxide powder	Sigma-Aldrich	CAS #1314-35-8
Selenium powder	Sigma-Aldrich	CAS #7782-49-2
Software and algorithms		
Origin 2018	OriginLab Corporation	https://www.originlab.com
MATLAB	MathWorks Co., LTD.	https://www.mathworks.com/products/matlab.html

RESOURCE AVAILABILITY

Lead contact

Further information and requests for resources and reagents should be directed to and will be fulfilled by the lead contact, Xuewen Fu (xwfu@nankai.edu.cn).

Materials availability

This study did not generate new unique reagents.

Data and code availability

- Data reported in this paper will be shared by the lead contact upon request.
- This paper does not report original codes.
- Any additional information required to reanalyze the data reported in this paper is available from the lead contact upon request.

EXPERIMENTAL MODEL AND STUDY PARTICIPANT DETAILS

This work did not need any unique experimental model.

METHOD DETAILS

Synthesis of the WO_x/WSe_2 heterostructures

The synthesis of the sample was carried out in a multitemperature-zone tubular furnace (OTF-1200X-II) equipped with a 1 in. diameter quartz tube. A powder mixture of 6 mg NaCl (99%, Sigma-Aldrich) and 60 mg WO_3 (99.9%, Sigma-Aldrich) in an aluminum oxide boat was placed in the center of second zone. SiO_2 (260 nm)/Si substrate was placed on the alumina boat with the surface facing down. The Se (99.99%, Sigma-Aldrich) powders were placed in a separate aluminum oxide boat (wrapped with iron wire at the front end) at the upper stream side in the first zone, and we can control the position of the aluminum oxide boat in the first zone within a certain range through the outer magnet. The first and second zone of the furnace was heated to the growing temperature (300°C and 900°C) with a ramp rate of 10 °C min^{-1} and 30°C min^{-1}, respectively. The pressure within the furnace was controlled through the needle valve at the front end of the vacuum pump. Ar (or Ar/H$_2$) with a flow rate of 50 (or 50/5) sccm (cubic centimeters per minute) was used as the carrier gas. The furnace was allowed to cool down naturally.

Characterizations of WO_x s-MW and WSe_2 film

The optical images and secondary electronic images were taken with optical microscopy (OM, Leica DM2700M RL) and scanning electron microscope (SEM, Thermofisher Quattro S). Energy dispersive X-ray spectroscopy (EDX) elemental mapping was taken from a SEM (Zeiss Merlin Compact) instrument equipped with EDS (Oxford X-max50). In addition, Raman and PL spectroscopy (HORIBA LabRAM ODYSSEY) with visible laser light (λ = 532 nm), were used to characterize the optical properties of the WO_x s-MW and WSe_2 film. Transmission electron microscopy (TEM) images and SAED were taken from a TEM (Talos F200i) instrument.

Nonlinear optical performance measurements

All SHG measurements were acquired by a mode-locked YAG laser (Spectra-Physics Spirit 1030-100) at 800 nm (Orpheus-3H, pulse width of 30 fs, repetition frequency of 50 kHz). For the polarization-dependent SHG pattern, the collimated laser beam was passed through a λ/2 wave plate (WPHSM05-808, Thorlabs) to change the detection angle. All our experiments were carried out at room temperature.

QUANTIFICATION AND STATISTICAL ANALYSIS

Figures shown in the main text were produced by Origin 2018 and Microsoft PowerPoint from the raw data.

ADDITIONAL RESOURCES

There are no additional resources needed to be declared in this manuscript, additional requests for this can be made by contacting the lead contact.